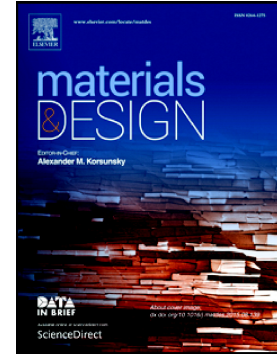


Accepted Manuscript

Microstructural characterisation of a nickel alloy processed via blown powder direct laser deposition (DLD)

Jonathan Jones, Mark Whittaker, Ross Buckingham, Richard Johnston, Martin Bache, Daniel Clark



PII: S0264-1275(16)31588-X
DOI: doi: [10.1016/j.matdes.2016.12.062](https://doi.org/10.1016/j.matdes.2016.12.062)
Reference: JMADE 2607
To appear in: *Materials & Design*
Received date: 14 November 2016
Revised date: 19 December 2016
Accepted date: 22 December 2016

Please cite this article as: Jonathan Jones, Mark Whittaker, Ross Buckingham, Richard Johnston, Martin Bache, Daniel Clark , Microstructural characterisation of a nickel alloy processed via blown powder direct laser deposition (DLD). The address for the corresponding author was captured as affiliation for all authors. Please check if appropriate. *Jmade*(2016), doi: [10.1016/j.matdes.2016.12.062](https://doi.org/10.1016/j.matdes.2016.12.062)

This is a PDF file of an unedited manuscript that has been accepted for publication. As a service to our customers we are providing this early version of the manuscript. The manuscript will undergo copyediting, typesetting, and review of the resulting proof before it is published in its final form. Please note that during the production process errors may be discovered which could affect the content, and all legal disclaimers that apply to the journal pertain.

MICROSTRUCTURAL CHARACTERISATION OF A NICKEL ALLOY PROCESSED VIA BLOWN POWDER DIRECT LASER DEPOSITION (DLD)

Jonathan Jones¹, Mark Whittaker¹, Ross Buckingham¹, Richard Johnston¹, Martin Bache¹ and Daniel Clark²

¹*Institute of Structural Materials, Swansea University, Fabian Way, Swansea, SA1 8EN, UK*

²*Rolls-Royce plc, P.O. Box 31, Derby, DE24 8BJ, UK*

Abstract

A three dimensional structure of varying wall thickness has been manufactured from an alloy similar to 718 and subjected to metallographic characterisation. The technique is evaluated as a process capable of generating complex geometries. This can be used to add features or as a free form fabrication method. However, in order to allow for comparison to structures developed through more traditional techniques, detailed microstructural characterisation has been undertaken to attempt to understand the potential effect of variation on resultant mechanical properties.

Samples were extracted from six locations with different wall thicknesses, intricate features and intersecting ligament geometry. A γ'' linearly arrayed structure within a γ matrix was consistent throughout the component. Micro-porosity was restricted to isolated, spherical pores less than 1 μm in diameter. Electron back-scatter diffraction and X-ray computed microtomography quantitative microstructural analysis techniques have been utilized to assess the influence of layering upon microporosity, patterning and grain structure.

A detailed comparison is also made between blown powder Direct Layer Deposition (DLD) and a similar deposition technique, shaped metal deposition (SMD). Blown powder DLD produces a smaller weld pool and results in a more consistent microstructure than SMD, with less evidence of unfavourable phases brought about by prolonged exposure to high temperatures. The improved microstructure, however,

must be measured against the different process economics of the blown powder DLD technique.

Introduction

Nickel base superalloys typically consist of a matrix, the γ phase with a face-centred cubic (FCC) structure, plus a dispersion of ordered intermetallic precipitate “gamma prime” particles of the type Ni_3Al (γ'). [1] However, in niobium or tantalum rich alloys such as IN718, the principal hardening mechanism is provided via Ni_3Nb or Ni_3Ta “gamma double prime” precipitates (γ''). The γ'' is often presented as fine coherent platelets, as noted in parent plate IN718 material during a previous examination of IN718 SMD specimens, [2] or alternatively on previously formed γ' particles. The γ'' phase has a metastable body-centred tetragonal (DO_{22}) structure, transforming into coarse platelets of the stable orthorhombic (DO_a) δ phase (with identical composition) after prolonged exposures to temperatures above approximately 650°C .

Additive manufacturing allows additional design space which permits opportunities for high performance structures to be created from alloys of established chemical composition. Example structures which challenge traditional manufacturing are those with restrictions on line of sight such as annular box sections and enclosed webbed features. Limitations arise in predicting mechanical behaviour, where the material exhibits irregular or anisotropic responses. Typical work to date has focussed on macroscale characteristics which are needed to predict distortion and bulk trends.

Alloy 718 is widely used in many industrial applications as this established composition yields a comparatively weldable material with databases showing the potential for useful strength at elevated temperatures using conventional processing

routes.[3] A homogeneous structure with predictable isotropic mechanical response is a key enabler to the design and use of the high performance, topographically optimised structures which additive manufacturing offers.[4] The use of the alloy via deposition requires characterisation with respect to anisotropy.[5, 6]

In designing deposition strategies for additive technologies there are two principle issues, firstly the need for process stability to minimise scatter and secondly the need to physically deliver the combination of mass and energy over time to generate the evolving form. These two issues present a conflict which is considered in this article. Scatter in mechanical testing can relate to variations in microstructural distributions, such variations may occur in position, orientation and viewing plane.[7] Furthermore, the variations may manifest themselves in terms of morphology, phase and length scale. For laser and powder additive Ti6Al-4V, scatter in the fatigue test results near the endurance limit was attributed to a range of characteristic process flaws, sizes and locations.[8]

Microscale characteristics affect properties and component integrity. These may be considered as directional and stochastic, although the incidence and orientation may relate to the nature of build strategy and position in the build geometry. Previous work has characterised defects in powder bed structures.[9, 10] Micro level characteristics could include fissures, inhomogeneous segregate dispersion on solidification, and morphologies generated and disrupted by varying thermal excursions about the precipitate solvus experienced by the material volumes.[11]

In earlier work conducted by the authors, assessments of arc based SMD using TIG [12] and MIG [2], higher deposition rates were obtained due to the larger bead sizes of the consumable wire systems. However these methods had a coarser resolution

than can be achieved with a fine laser spot fed by powder, leading to implications for the subsequent machining envelope.

With the blown powder deposition process there is a potential for more geometrically complex components to be achieved, although the intricacy and precision of form comes at a cost in terms of deposition time. Metallic deposition, however, has the additional factor of differential heat accumulation which affects process stability, dimensional control and cooling rate. Key differences relative to the arc and wire techniques are the efficiency of consumable material utilisation in terms of powder capture in the pool.

When considering blown powder additive as part of a hybrid fabrication route, the lower rate of heat input can be beneficial in terms of the depth and degree of potential disruption and dilution. The process offers less deformation of substrate material generally, requiring less post process blending at intersections due to overbuilding.

Conceivably an entire component could be constructed rather than a hybrid approach. This offers the possibility to integrate additional component functionality rather than simply substituting a fabrication process. For example it may be possible to increase structural stiffness through fewer mechanical joints. Additional benefits might arise for vibration control, damping, specific strength, buckling resistance and ultimately fatigue strength. There are different thermal processing possibilities for hybrid or repair applications versus deposition of an entire component due to the potential option of a homogenisation treatment for the latter.

The process consistency is dependent on the control of the progressive height of the developing form with respect to the expected position in the toolpath for the deposition head.[13] Localised and layer on layer variation in layer height relative to the machine tool centre point challenge the deposition process spot size.[14] The pool

size may vary with the changing heat sink of the local section. Blown powder deposition has a variable powder capture rate according to the powder focus.[15] Within this framework, the process layer level consistency is affected by the process fill strategy (scan pattern and overlap). Characteristics for process control have been extensively covered previously.[16-19]

While location specific properties offer the potential for process tuning, location specific variations in heat sink and degrees of toolpath freedom can lead to process fluctuations which in turn yield microstructural variations. Micro scale mechanisms of deformation can significantly complicate predictions of component level behaviour under service load through the potential for complex strain pathways. An example of stress partitioning in a manner which would challenge predictive tools would arise through a varied ductility distribution. One might also expect creep variation with orientation as dislocation particle interaction may vary with orientation. In a cyclic loading condition there may be a varying potential for flaw interaction leading to microcrack coalescence with loading orientation.[20]

For the purpose of this study, a generic application with representative features was created. Geometric features were included which were close to the scale of the deposition beads, which in turn limited the options for microstructural disruption by layer on layer rotation.[21] The fine features linked sharply to thicker sections where a contour and hatch fill pattern could be used. Spur-like features and a partial enclosure were also incorporated.

The deposition strategy [7, 22-24] used here involved linear tracks of nominally 1mm wide beads, overlapped to form planar layers, with the deposition head normal to the layer increments. Where the geometry permitted, a layer on layer rotation was used with the intention to avoid the linear stacking trends exhibited as co-linear and co-

planar features noted in previous reports[11, 25]. Manipulation of the deposition head through accelerations and vector changes could also influence powder flow consistency which constitutes the mass input rate.

To assess the tendency for varied microstructural evolution using nominally constant, proprietary deposition parameters, this work has aimed to assess separate volumetric elements. The deposited structure was sectioned to enable detailed microstructural inspections at various locations throughout the build.

Experimental Procedures

Construction of the complex structures analysed in the current work were achieved through building in planar layers, using a commercial powder and common spot size, whilst varying the local revisit rate and fill pattern. Generally setup is broadly in line with industry, having constant spot size and powder feed rate, however specific process parameters are considered proprietary. The original locations of the six sections in relation to the complex blown powder DLD geometry are illustrated in Figure 1. These specific areas were selected because they provided samples of different wall thickness and examples of intersecting ligaments of different angular orientations. To aid interpretation of the current material, reference will be made where appropriate to previous work on the characterisation of IN718 shape metal deposition (SMD) materials. [2, 26]

The structure was supplied in the as processed blown powder DLD condition. The structure was extracted using mechanical cutting and subjected to a standard two stage precipitation treatment under high vacuum conditions (10^{-6} mbar), [2].

PRECIPITATION TREAT : 720°C / 8 hours.

FURNACE COOL : 55°C / hour to 620°C / 8 hours / Air cool.

The six specimens were sectioned at the same build height and polished using standard metallographic techniques and underwent a final chemical polish with an aqueous suspension of colloidal silica containing 20% H_2O_2 (Hydrogen Peroxide). Specimens were examined under optical microscopy for evidence of porosity prior to etching using a Reichart optical microscope with an attached Nikon CoolPix digital camera. Subsequently, specimens were etched with a solution of 10ml HNO_3 , 20ml HCl , 25ml distilled water and 10ml hydrogen peroxide (H_2O_2) for approximately 150 seconds.

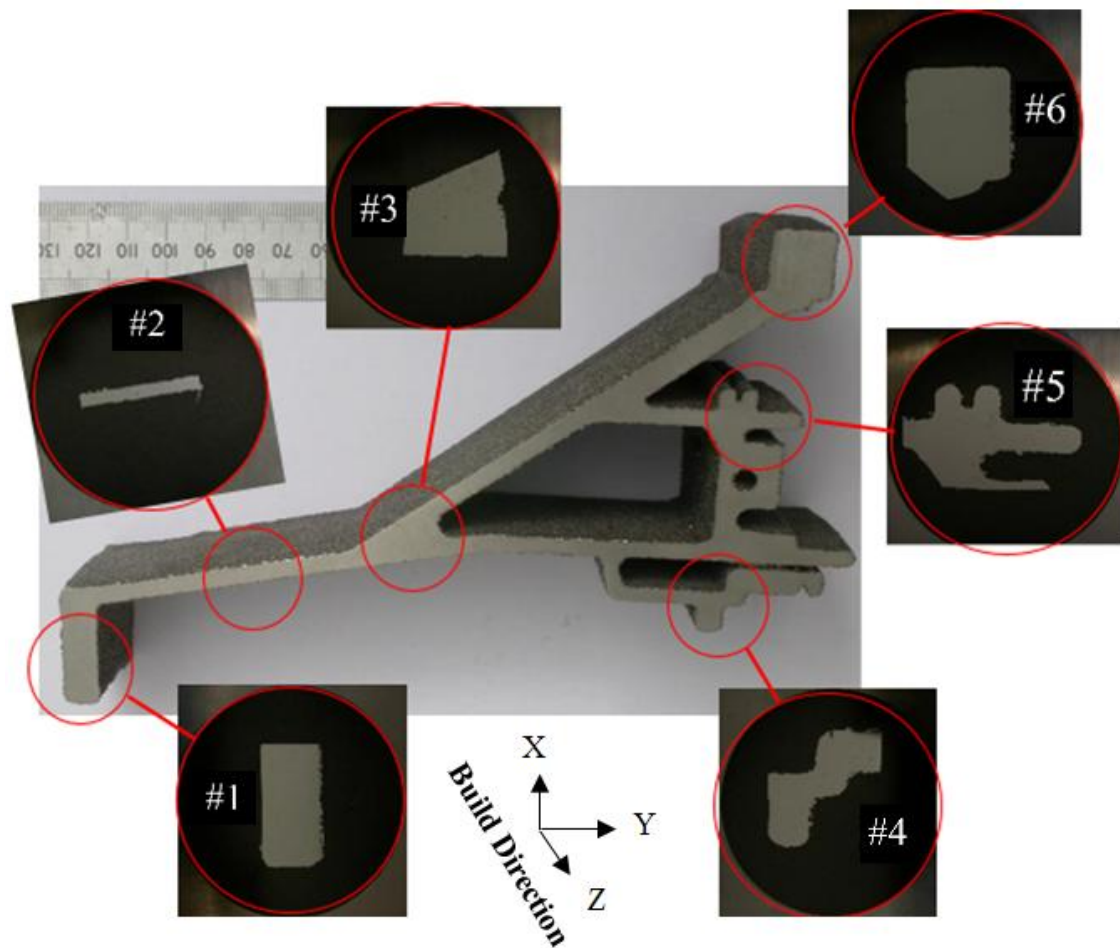


Figure 1: Blown powder DLD structure with locations for the six metallographic specimens, #1 - #6. The X, Y and Z (build direction) axis of epitaxy are given.

In contrast to a previous investigation on IN718 SMD materials, [2, 26] on this occasion it was noted that this etching procedure was consistently successful on all

specimens, suggesting more electrochemical uniformity. Microstructural analysis was performed on both a Jeol 6100 SEM and Phillips XL30CP SEM. High resolution images of the microstructure were recorded using a HKL Flamenco software package attached to the SEM. Chemical analyses were performed using a Jeol-35C SEM fitted with an Oxford Instruments EDX X-ray dispersion facility.

Two orthogonal sections were prepared from each specimen, the first in the X-Y plane as viewed in Figure 1, the second in the orthogonal X-Z plane. It became evident, however, that no significant differences in the microstructure were detected in the different orientations. To effectively describe the dendrite morphologies within the microstructure quantitatively, the length of the average primary dendrite axes (PDAS) and the secondary dendrite arm spacing (SDAS) has been measured. Finally, Vickers hardness measurements were taken from each specimen, employing a load of 10 Kg. Hardness measurements were taken traversing the minor axis of the specimen at regular intervals to investigate the macroscopic homogeneity of the material.

To investigate the microstructure under electron backscatter diffraction, samples were mounted in conductive Bakelite and polished using standard metallographic techniques described previously, however, with a final polish of 15 minutes using 0.04 μm colloidal silica. Two electron back-scatter diffraction (EBSD) maps were completed upon specimens #2 and #6 at 200x magnification, allowing at least 50 grains to be analysed. On completion of data acquisition the two maps were stitched with an overall indexing rate of 99% before cleaning.

X-ray microtomography (μCT) scans were completed on Specimen #2 using a Nikon XT H 225 microfocus X-ray tomography system, with a 1.3 Megapixel Varian PaxScan 2520 amorphous silicon flat panel digital X-ray imager, in reflection mode with a tungsten target. An X-ray tube voltage of 160 kV, a source current of 150 μA ,

with an exposure of 1415 ms, averaging 1429 projections, resulted in an isometric voxel (3-D pixel) size of 3.53 μ m. The tomograms were reconstructed from 2-D projections using a Nikon cone-beam reconstruction algorithm and proprietary software (CTPro version 3.0, Nikon Metrology). The commercial software VGStudio Max 2.1.5 and Avizo Fire were used to view the reconstructed data, 2-D grey scale slices/planes, and rendered 3-D volume. The sample size and imaging configuration resulted in a total scanned volume of $\approx 9.241\text{mm}^3$.

Porosity was segmented from the IN718 by isolating the portion of greyscale voxel-intensity histogram within the visualisation software which relates to air. Variations in greyscale values are due to the difference in X-ray attenuation of the constituent materials and gas/air imaged within the volume. As this was performed on digital sub-sample regions of interest within the sample, the air relates only to the porosity, and not the air surrounding the sample.

Results

Compositional Analysis - EDX analysis was employed, to sample the base γ material and γ'' phases. A comparison between the chemical constituents within the blown powder DLD material in this study and the standard specifications of IN718 is given in Table 1.

Table 1: EDX chemical composition results, comparison between blown powder DLD and conventional cast IN718, [3], At%

Alloy	Ni	Fe	Cr	Nb	Mo	Ti	Al	Co
DLD	53.61	17.87	19.51	5.26	1.69	1.05	0.58	0.44
CAST 718	50-55	13.5-23.5	17-21	4.75-5.5	2.8-3.3	0.7-1.15	0.2-0.8	≤ 1

Metallographic Examination - No significant variations were noted through the thickness of the component at any of the six locations. The typical grain structure within all specimens is given in

Figure 2. The typical γ'' (cored structure within γ matrix can be seen in Figure 2a). Individual grains are defined by the juxtaposition of γ'' cores of different orientations,[27] in Figure 2b). The nature of the γ'' cores was confirmed through the input of appropriate lattice parameters into the EBSD software. This diversity in solidification vectors is distinct from epitaxial laser metal forming E-LMF [28]. Two dimensional γ'' cores can be seen in Figure 2c), whilst in Figure 2d) a higher magnification images reveals the γ'' cores to be associated with γ' or carbides.

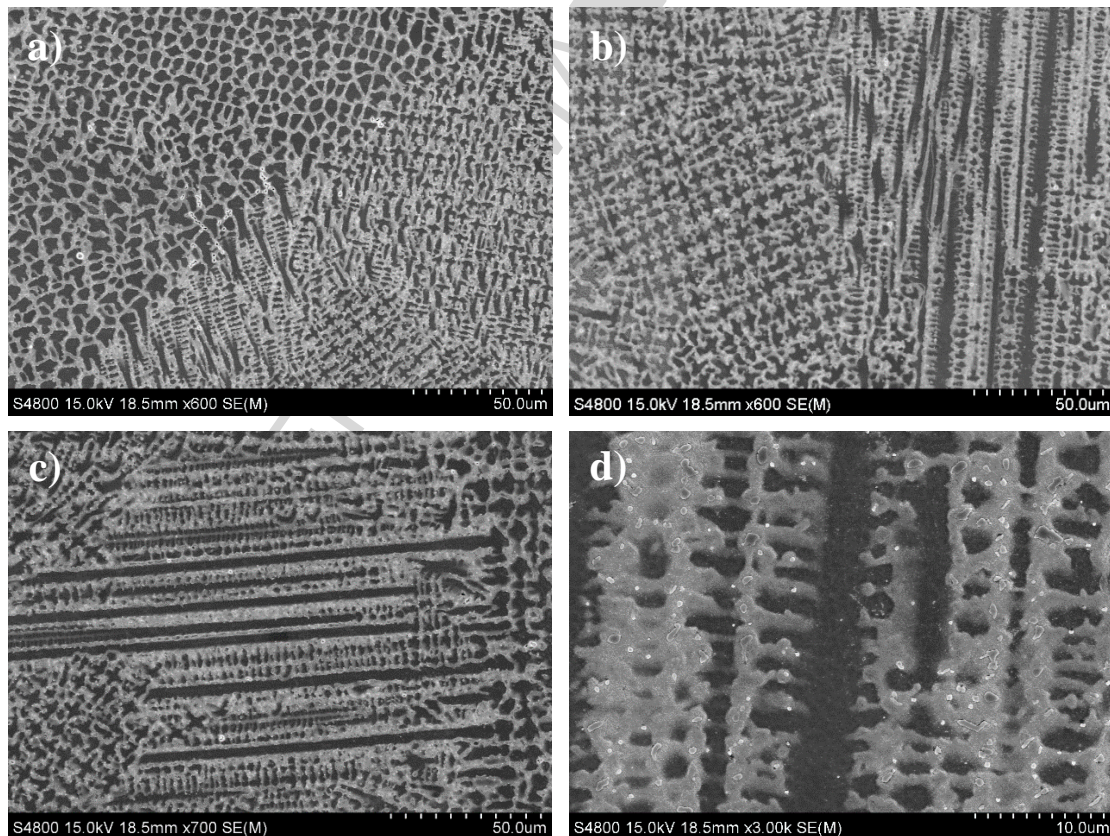


Figure 2: Typical microstructure of the IN718 blown powder DLD component within this study. a) γ'' cored microstructure within γ matrix; b) Grains defined by the juxtaposition of γ'' cores of different orientations; c) Two dimensional γ'' cores; d) γ'' cores associated with γ' or carbides.

To characterize the morphology of dendrites, results of the primary and secondary arm measurements across the six specimens are summarised in Table 2 and Table 3. Examples of primary dendrite arm spacing measurements are given in Figure .

Table 2: Primary dendrite axis length measured, across the six specimens.

Specimen	Average Count	PDAS μm			Average Count	PDAS Triangle μm		
		Average	Max	Min		Average	Max	Min
#1	20	9.25	9.84	8.65	29	5.48	4.02	7.31
#2	25	5.03	6.43	3.26	25	7.36	9.33	5.74
#3	23	5.54	6.69	4.46	18	6.53	8.69	5.19
#4	26	5.77	7.06	3.74	24	5.27	6.76	3.83
#5	19	6.83	7.80	4.91	23	6.16	7.84	3.49
#6	22	7.03	9.66	4.21	25	6.47	8.54	4.88

Table 3: Secondary dendrite arm spacing measured, across the six specimens.

Specimen	Average Measurement		SDAS Average μm
	Count	Length	
#1	7.2	16.0	2.1
#2	9.4	26.5	2.8
#3	9.3	17.7	1.9
#4	12.7	31.0	2.4
#5	11.3	20.3	2.1
#6	10.6	25.5	2.4

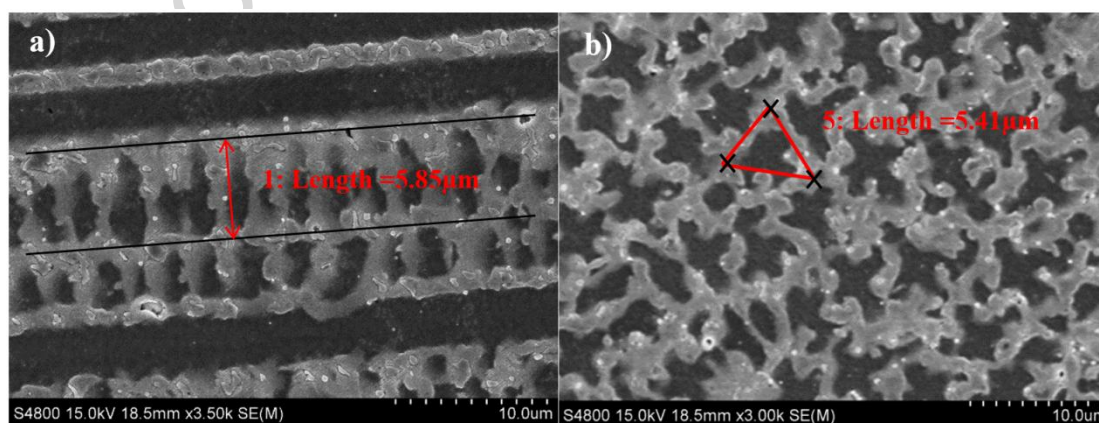


Figure 3: a) Example of primary dendrite measurements taken from specimen #2; b) Triangular method of measuring primary dendrite axis, specimen #5.

X-ray Microtomography – A limited volume of micro-porosity was found throughout the sampled material. X-ray μ CT results show the typical morphology of the micro-porosity to be spherical, with pores never exceeding 0.37mm^3 in volume and 0.13mm in diameter. This morphology and size found was consistent with analysis under an electron microscope upon a polished cross section of specimen #2. The total volume of micro porosity measured was equivalent to just under 0.095% of the total volume of specimen #2.

The electron microscope image and μ CT 2D slice/plane view in Figures 4a) and 4b) respectively, outline the typical morphology of large pores formed during powder atomisation. The majority of the pores, > 98%, were less than $\sim 25\mu\text{m}$ in diameter. Illustrated in Figure 4c is a 3D iso-surface representation of the identified porosity found within specimen #2 via μ CT, with quantitative data tabularised and represented via a histogram in Table 4 and Figure 5 respectively.

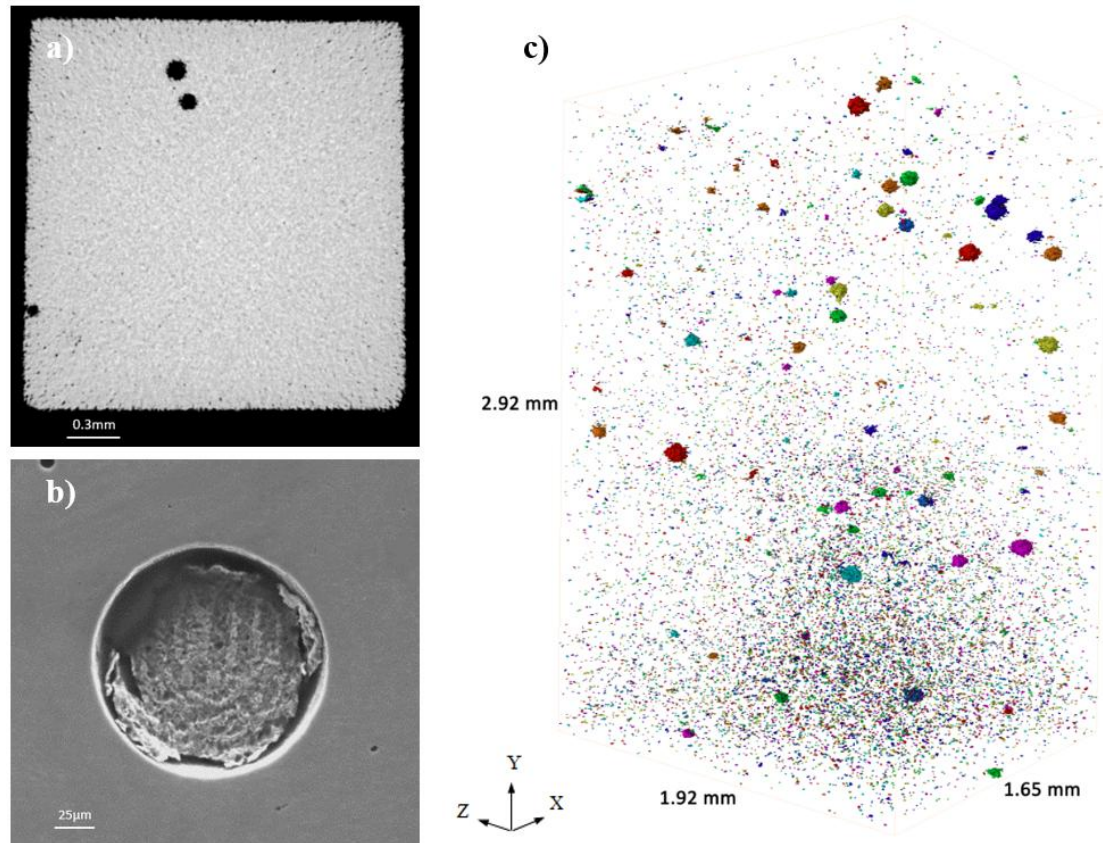


Figure 4: a) An X-ray μ CT 2D slice/plane view of pores in specimen #2. b) Electron microscope image of a pore found in specimen #2 with a seemingly spherical morphology. c) A 3D iso-surface representation of all micro-porosity within specimen #2, $> 7\mu\text{m}$ in diameter.

It should be noted that the accuracy for detecting smaller pores closer to the voxel size, and accurately determining the diameter of these pores is limited due to modulation transfer function blurring effect and partial volume effects [29, 30].

To overcome this issue with pore measurements, a threshold could be set for the minimum detected pore diameter that can be included in the analysis. In this case, it is equivalent to two adjacent pixels in a given direction, equalling a threshold of $7\mu\text{m}$ in diameter and above. Therefore, quantifications of the total porosity can be assumed to be a lower bound, but this would expect to generate only a slight underestimation as these very small pores contribute little to the overall pore volume.

Table 4: Results of X-ray μ CT micro porosity analysis on specimen #2.

Pore	Specimen #2
Number	18131
Average ϕ (μm)	11.8
Maximum ϕ (μm)	123.9
Average V (μm^3)	0.5
Maximum V (μm^3)	368.9

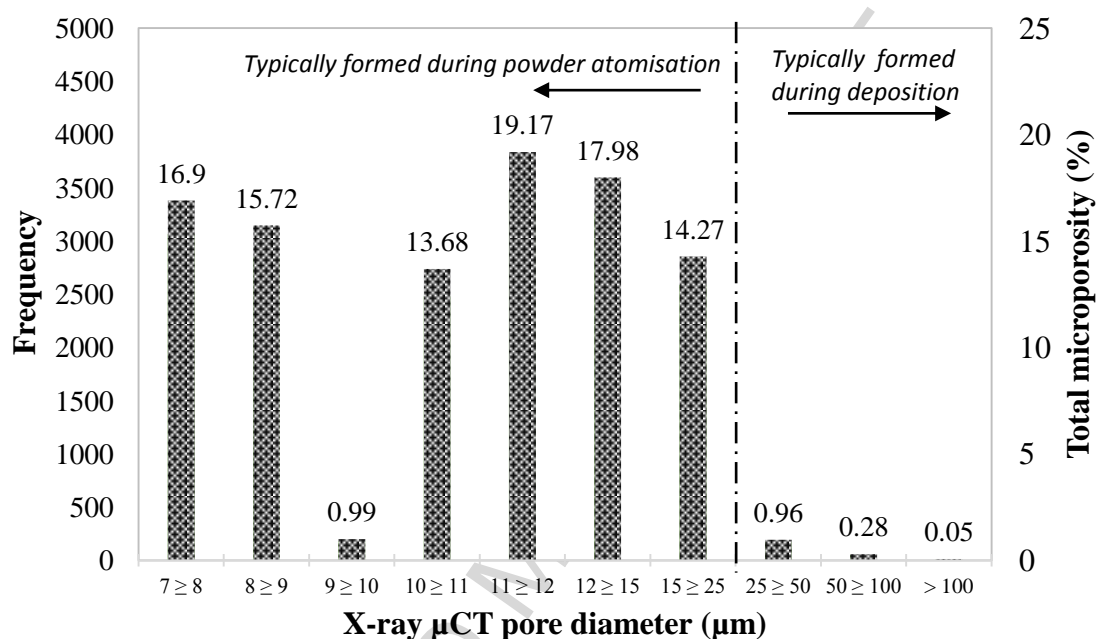


Figure 5: Histogram pore diameter and frequency under X-ray μCT in specimen #2

Hardness - Three Vickers hardness measurements together with the calculated average for each specimen are presented in Table 5. Clearly, good consistency is noted between the data irrespective of location in the component.

Table 5. Vickers hardness measurements.

	Indentation #1	Indentation #2	Indentation #3	Average Hv
Specimen #1	458	466	435	453
Specimen #2	436	454	436	442
Specimen #3	452	437	443	444
Specimen #4	444	441	429	438
Specimen #5	442	440	429	437
Specimen #6	443	438	450	444

Electron Back Scatter Diffraction - Micro-texture measured from a relatively thin and simple build geometry, specimen #2, was compared to that of a thicker and complex build geometry, specimen #6. Initial analysis of the texture was conducted using both IPF and pole figures with both showing a very weak texture and no distinct orientation dominating in both the regions investigated. However, comparison of the pole figures between the two regions did indicate a slightly higher degree of texture in the thicker specimen #6, preferably orientated towards the (100) plane.

This is likely related to the larger degree of columnar growth seen in the area, discussed in greater detail later. It is also supported by subsequent ODF analysis which shows an increased intensity close to rotated cube. The thinner specimen #2, shows an increasingly disrupted texture from both the pole plots and ODF figures which show lower intensity with a wider distribution. This is consistent with the finer more equiaxed grain structure seen in the thinner specimen as a result of higher cooling rates inhibiting grain growth.

Fiber texture analysis is shown in Figure 6 and Table 6, where the reference direction is //X which is assumed to be the deposition direction. The $\langle 100 \rangle$ and $\langle 110 \rangle$ fiber components were dominant in the thicker specimen. Within the thinner specimen the $\langle 111 \rangle$ fiber component is of the highest concentration and is typically the dominant orientation most likely to twin owing to its relationship with the widely known copper texture component (112) $\langle 111 \rangle$. It is evident from the texture analyses that the degree of overall orientation during layer deposition is dependent on the cross-section thickness.

a) #6 Thick Section

b) #2 Thin Section

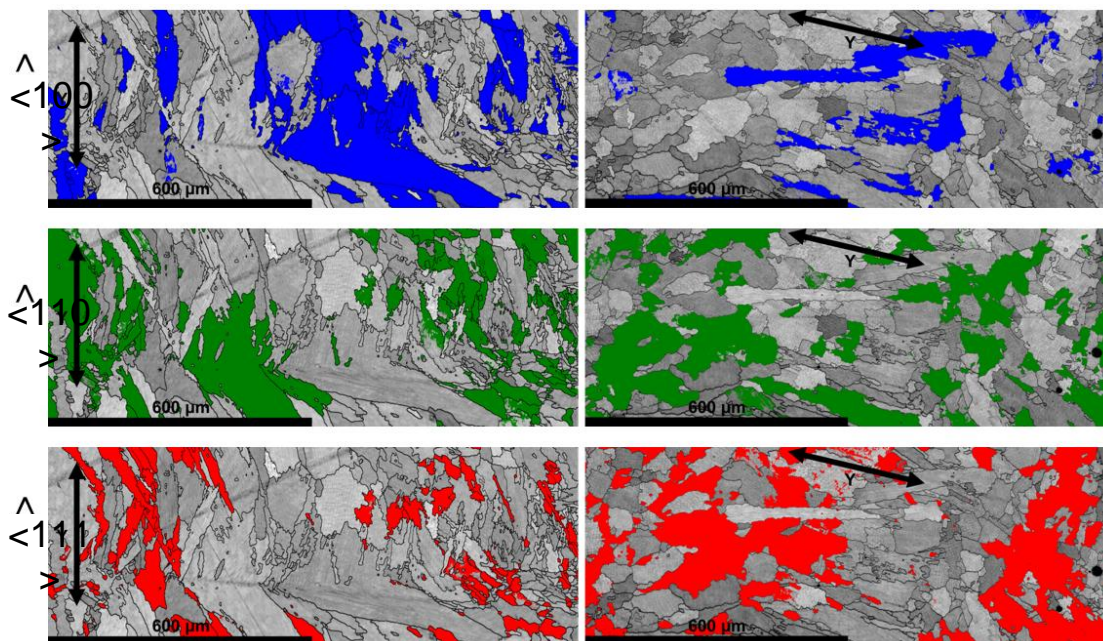


Figure 6: Fiber texture analysis for a) specimen #6 a thick section; b) specimen #2 a thin sections.

Table 6: Fiber texture analysis results

Fiber Component	Specimen #6 (%)	Specimen #2 (%)
<100>	28.9	11.3
<110>	29.6	29.0
<111>	15.4	31.3

Within the relatively thick specimen the larger columnar grains show the lowest levels of misorientation, with the finer grains showing the highest, tabularised grain size analysis results are given in Table 7. In comparison, the thin specimen shows a more even distribution of misorientation grains with most having misorientation $\leq 2^\circ$. The two specimens both showed large amounts of internal local misorientation within the grains which correlated to the layered morphology seen in forward scatter imaging.

Table 7: Grain size analysis.

Grain Size (μm)	Specimen #6 (Thick)	Specimen #2 (Thin)

Maximum	377.9	138.8
Minimum	5.0	0.6
Average	25.4	16.0
Std. dev	33.0	22.6
Aspect Ratio		
Maximum	1.0	1.0
Minimum	16.3	10.6
Average	2.6	1.9

Grain boundary analysis of the two specimens showed the majority of the grain boundaries to be of high angle ($>15^\circ$) with no significant subgrain formation. Both maps also showed no significant twinning and an almost random grain boundary distribution. The thicker specimen showed the highest average grain size $\approx 9\mu\text{m}$, greater than that of the thinner specimen, with a higher average aspect ratio at ≈ 0.7 . The distribution supports this and shows the thicker specimen contained fewer finer grains whilst having the largest grain size, a result of the large columnar grains seen in the EBSD maps previously.

Discussion

In seeking to assess the effectiveness of the blown powder DLD process in IN718, it is clear that process parameters which affect melt pool temperature result in detectable microstructural changes which have the potential to alter mechanical properties. The current study has sought to characterise the development of microstructure as a function of geometric form. Clearly, several factors affect melt pool temperature [31]. The process energy has been shown to affect solidification and cooling rates and since

alloy 718 is sensitive in terms of development of alternative phases and microstructural form, any variations have been closely monitored.[32] However, the microstructure of all the specimens in this study appeared to be relatively consistent and insensitive to differences in component wall thickness or orientation of the metallographic section as viewed under optical and SEM microscopes.

Dendrite arm spacing will significantly affect microstructural development through the chemical dispersion of precipitation forming elements and as such the current work sought to evaluate quantity and directly compare it with more established processing methods. Primary dendrite arm spacings of 5 μm were reported in previous work, [33] where the authors had used a higher power system with a larger spot size. However, using similar settings to these authors, other groups have reported a primary dendrite arm spacing of 11.5 to 38.0 μm , clearly demonstrating the sensitivity of the microstructure with regards to process settings.[34] Previous work has investigated the variation in grain size through blown powder processes, for different alloys. The grain size was reported to be varied by altering the spot size, travel speed and or laser power to change input power and solidification rates.[21, 35-37]

In the current work, primary dendrite arm spacing of 3 to 10 μm was regularly detected in the blown powder DLD material allowing for the development of a controlled microstructure which would be expected to provide relative homogeneous mechanical properties. However, in certain instances the PDAS measurements taken from the opposing from techniques delivered contrasting results, possibly due to the depth at which the cross section passed through the dendrites. Overall the triangular PDAS measurements were less consistent than the conventional method.

The PDAS measured in this work has been compared to previous literature using selected additive and conventional blown powder processes (variant of the theme of a travelling heat source on an arm, using blown powder), Table 8. The techniques include commercially processed (CP), selective laser melting (SLM), direct laser forming (DLF), laser rapid forming (LRF), laser solid forming (LSF). All PDAS measurements were taken using the conventional DAS measurement technique.

Table 8: Conventional dendrite cell size comparison across diverse additive processes

Processing Technique	Cast ^[32]	CP ^[38]	SLM ^[7]	DLF ^[39]	LRF ^[33]	LSF ^[34]	DLD
DAS (μm)	10 - 40	~ 5	~ 0.7	5 - 8	~5	11.5 - 38.0	3 - 10

When considering chemical analysis of the blown powder DLD material, it should be noted that, due to the fine scale of the structures sampled relative to the volume of the X-ray beam, any quantitative values may be subject to significant experimental error. Despite this limitation, the EDX measurements remain valid as a tool to show relative differences in composition. With this in mind, the γ phase appeared to be depleted in niobium relative to the ordered γ'' precipitate, with niobium contents approaching 10% in the γ'' phase. This evidence alone supports the assumption that the cored structure is indeed γ'' material and is consistent with material processed using more conventional methods, e.g. casting.

However, the present results were also compared to similar data taken from IN718 SMD material, in which distinct Laves in addition to δ - γ'' phase had been identified [2, 26]. It was found previously that the niobium content of the Laves phase was considerably higher than that found in the proposed δ - γ'' phase. This is in accordance with theory as Laves is comprised of Ni_2Nb whereas the δ - γ'' phase contains

predominantly Ni_3Nb . A direct comparison was available between the chemical compositions of the present γ'' solidification cores and the δ - γ'' phase in the IN718 SMD, since these two precipitates should represent the two allotropic forms of γ'' . The EDX analysis of these two precipitates provided similar niobium content in each, i.e. close to 10%.

Gas entrapment found in alloy 718 deposits has been linked to the gas atomisation process typically employed to produce the stock powder [33]. X-ray μCT has been used to examine pores in additive structures [20, 40-42]. In a similar planar build additive process, aligned pores have been seen with both vertical and horizontal scan passes [43]. An alternative mechanism for void formation, with a different scale and morphology in the blown powder build, is through holes generated via irregularity in the clad bead profiles [31].

Results of the X-ray μCT analysis describing the porosity within the IN718 blown powder DLD component were encouraging with the technique being able to clearly visualise the micro porosity present. Limited micro-porosity was observed associated with the precipitates, whilst within the matrix material any porosity seen was in the form of entrapped gas pores as previously described. The 3D iso-surface representation of all micro-porosity in Figure 4c) appears to show a non-uniform distribution of smaller pores, $\varnothing < 25\mu\text{m}$ typically formed during powder atomisation, with regions of the specimen having larger concentrations than others.

Clearly, aligned or co-planar arrayed porosity may prove detrimental to mechanical properties due to localised crack linkage or anisotropic constitutive behaviour. However, no evidence of aligned porosity or lack of fusion between the build pattern and or scan planes was detected, at the porosity resolution of these scans. This is

outlined in the 3D iso-surface representation of larger micro-porosity, $\phi > 25\mu\text{m}$, throughout the assessed specimen, typically formed during solidification in Figure.7.

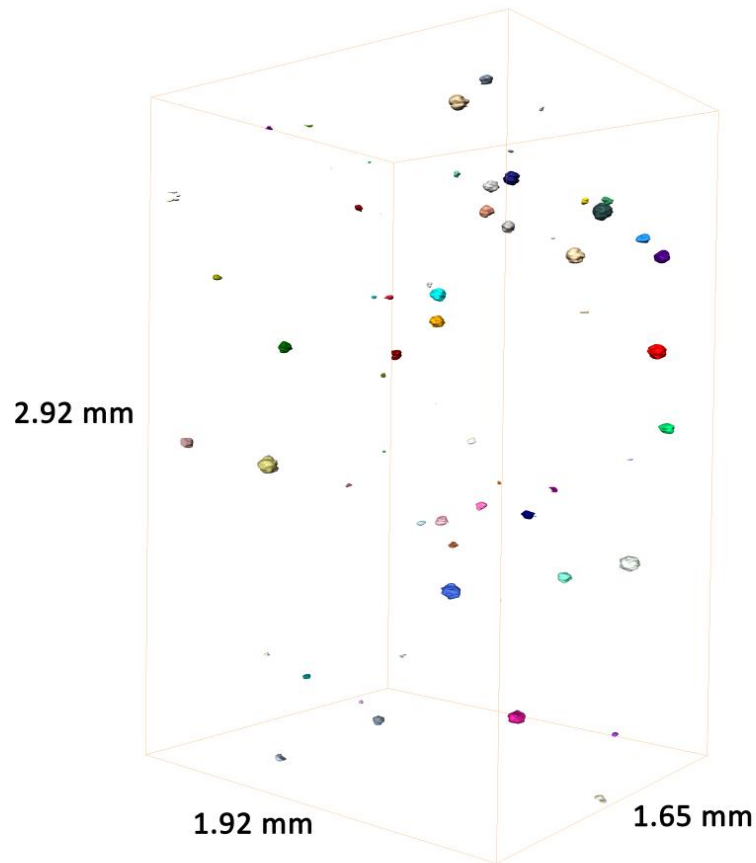


Figure 7: Visualisation of the 3D tomogram for micro porosity with $\phi > 25\mu\text{m}$ in specimen #2 with dimensions of the scanned volume in mm.

Table 9: Structural criteria noted in the present blown powder DLD 718 material.

Discontinuity type	DLD 718
Cracks	None Found
Start or end crater	None Found
Oxidation	None Found
Isolated porosity	0.12mm
Grouped porosity in plane section	0.21mm
Grouped defects defined volume used	2

Typically pores formed during powder atomisation on ranged from 1 to $2\mu\text{m}$ diameter whilst large pores, 30 to $200\mu\text{m}$, [20, 26, 28, 44] were formed during deposition.

Structural criteria proposed for alloy 718 components can be found in [6]. The characteristic processing flaws found in the blown powder DLD 718 during this study are compared to the same criteria in Table 9.

Carbides were evident within the structure, but were generally sub-micron in scale and well dispersed, with no particular segregation within grains towards grain boundaries (which may prove detrimental to fatigue performance). The scale of carbides was generally smaller than observed in typical wrought IN718, however, it is not expected that this would significantly alter mechanical properties. Ideally any carbides present should be small and evenly distributed along grain boundaries so as to provide Zener pinning and inhibit time dependent damage mechanisms, therefore the processing route investigated here could be optimised further for performance with respect to creep. However with developments in 5-axis toolpaths, more variations in mesoscale and microscale features can be expected. [45] The additional tooling axes result in less planar layering as they generate more complex build strategies and geometries leading to more complex cooling orientations. [36]

Consistent hardness values sampled throughout the material support the previous assumption that a well dispersed carbide distribution along with the dendrite morphology reported is representative of homogeneous properties throughout the blown powder DLD material. Hardness results are given in Table 10, where a comparison is made between blown powder DLD, SLM, LMD and standard processing techniques [7, 24, 46, 47]. It can be seen that hardness values from blown powder DLD material compare favourably with other processing methods. This may indicate a general uniformity of the precipitate dispersion or a coarseness in sampling relative to the spatial distribution due to the repeated remelting and resulting superposition of heat affected zones.

Although the material appears isotropic and homogeneous based on both microstructural observation and hardness profiles, it is clear that grain size and orientation needs to be more closely considered, particularly due to the possibility of localised anisotropy and inhomogeneity providing opportunity for crack initiation. In particular, migrating grain boundaries through recrystallisation with repeated thermal excursions have been associated with cracking mechanisms [48]. Therefore, the particular aim of the EBSD studies in the current work was to determine any effect on the microstructure of; varying scan path frequency, varying fill pattern, interval, orientation layer on layer and cooling rate (thick / thin sections).

Table 10: IN718 Vickers micro-hardness (Hv) measurements from different process variants.

Processing method	DLD	SLM ^[7]	LMD ^[24]	Forged ^[46]
As-deposited		291	~ 242	
Solution treated		423	~ 210	170-250
Precipitation hardened	446	410	~ 432	~ 400

It is assumed that the overall level of recrystallisation does not change with section thickness but that variation in the growth rate of grains leads to the inhomogeneous grain size, with similar studies reporting average grain size after a recrystallization treatment of 200 μ m.[20]

The preferred growth of these grains is likely to occur along the cube (100) planes parallel to the direction of laser deposition and the associated dynamics of the solidification front at the sloped rear edge of the melt pool. Fiber texture analysis has shown the <100> and <110> fiber components to be dominant in the thicker specimen. The <100> direction is known to be the preferred solidification direction of FCC materials and this would explain the affinity to the larger columnar grains where cooling rates are slower due to the heat retention in the larger material bulk.

The $\langle 110 \rangle$ fiber also shows a well-defined texture and is associated with deformation and recrystallisation mechanisms in conventionally processed materials. However, further research is required to determine its dominance in blown powder DLD processing. Nevertheless, it is suggested that the longer time period between each pass in this structure allows for increased levels of cooling, limiting the level of grain growth following recrystallisation of newly deposited material.

The difference in grain size between the sections of varying thickness is given in Table 7. This is probably a direct result of the varying heat retention in conjunction with subsequent cooling rates. A variation in the thickness of the specimens leads to this lack of homogeneity by allowing for greater degrees of grain growth in the thicker regions. The thicker sections also contained more directionally solidified grains where the major axis of the columnar grains tended to form perpendicular to the deposition path as a result of thermal gradients leading growth to more vertical orientations, typical in layered metallic components.

Grain boundary analysis of the two specimens, Figure 8, showed the majority of the grain boundaries to be of high angle with no significant subgrain formation. The lack of subgrain growth would suggest that dynamic recrystallisation is dominant with minimal dynamic recovery and therefore no significant residual mechanical strains should be present in the heat treated state. This may be due to the limited size of the sample investigated. Special boundary analysis of both areas also showed no significant twinning and a close to random grain boundary distribution.

The larger columnar grains within the thick specimen #6, showed the lowest levels of misorientation with the finer grains showing the highest as a result of the higher grain surface area. If given more time at heat treatment temperature it is assumed that these

smaller grains would be consumed by the larger columnar grains, thus minimising internal grain misorientation.

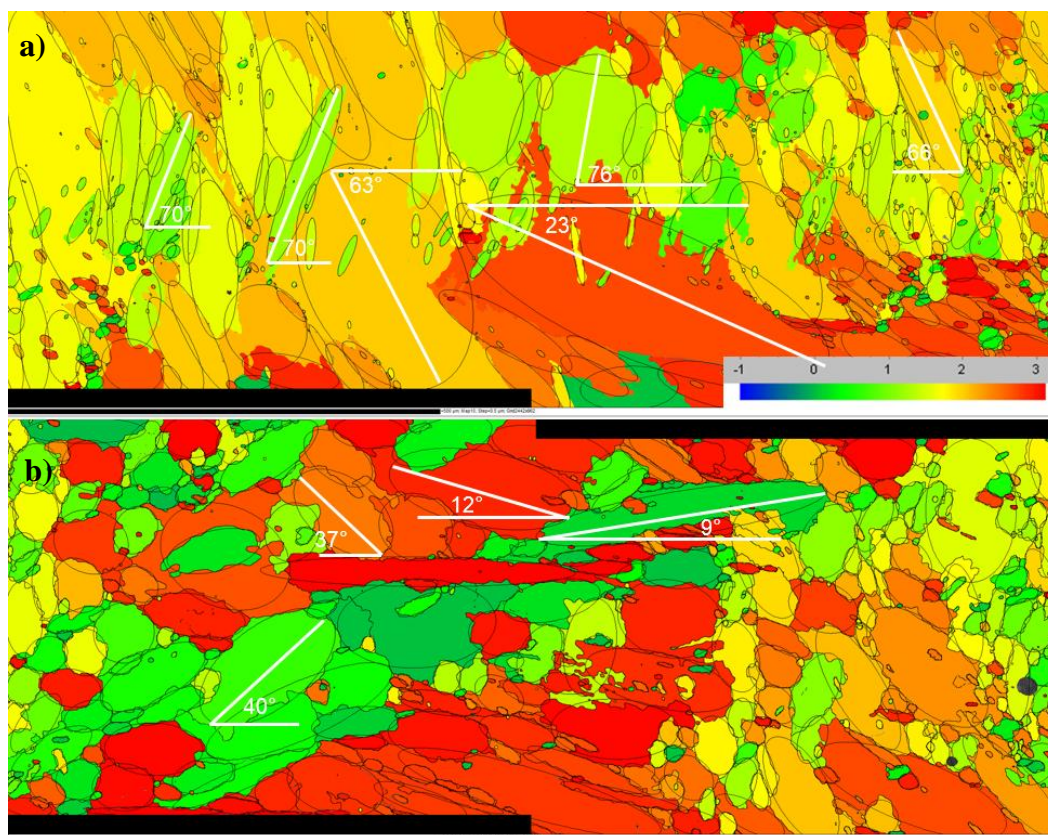
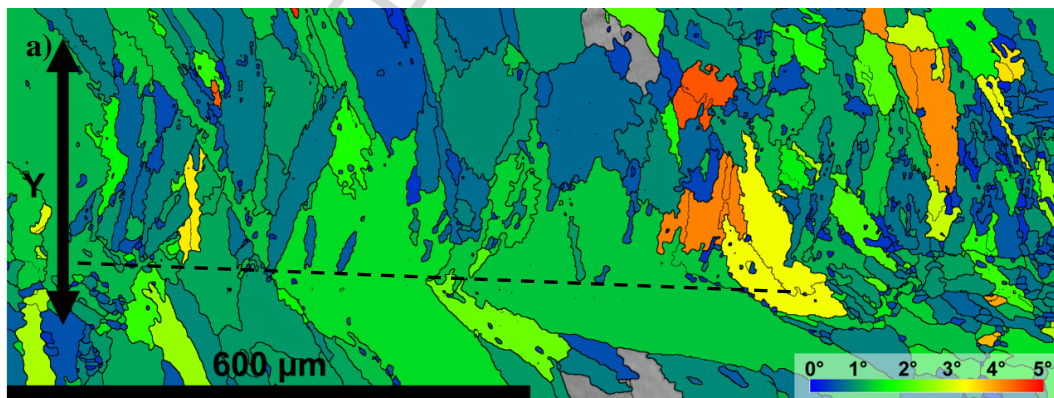


Figure 8: Grain boundary analysis of a) specimen #6, thick b) specimen #2, thin.

The thinner specimen showed a more even distribution of misorientation within grains, $\leq 2^\circ$ as would be expected for the more unimodal grain size distribution. The presence of the columnar grains would suggest a microstructure of greater recrystallised grains which have been able to grow at the expense of the smaller grains. This is again a likely result of greater heat retention in specimen #6 as a result of the section thickness the local heat source visitation rate allowing for greater amounts of grain nucleation and growth, therefore reducing the average grain misorientation. This is in agreement with the findings of the grain boundary assessment.

Trends in any patternation were difficult to determine as a large area of investigation via EBSD is not practical, given the resolution required for accurate data acquisition. The thicker geometry, however, did show a less spherical grain structure with some evidence of herringbone type patterning where the major grain axis was on average 20° from the layering direction. The thinner geometry showed a greater variation in orientation of the major grain axis with regards to layering direction. The EBSD map does contain some elongated grains approximately parallel to the layering direction but contains a significant proportion of spherical grains with no notable orientation pattern.

There appears to be interpenetration of columnar grains from two growth axes, noted just above the dotted line superimposed in Figure 9. This appears to indicate two competing growth axes. No obvious bands of coarse grains and fine grains were observed in the microstructure as shown in **Error! Bookmark not defined.** and in contrast to examples within the literature [21, 49, 50].



b)

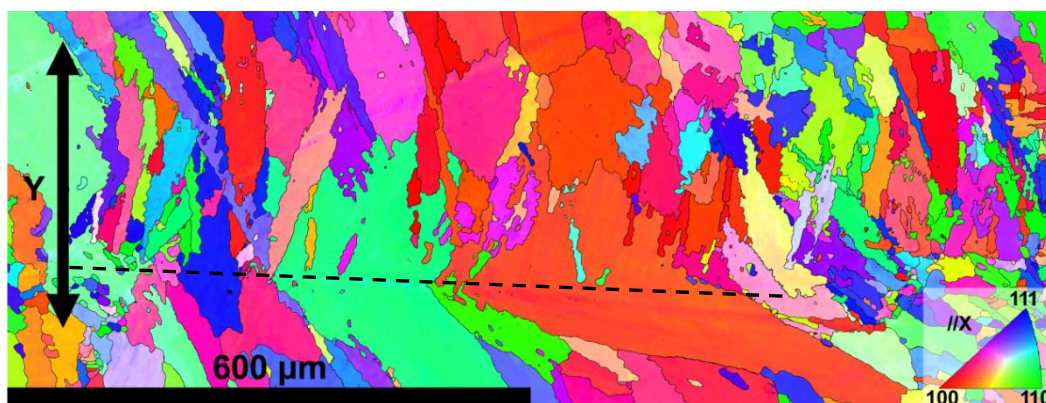


Figure 9: Microstructural detail of specimen #6; a) Grain misorientation (Maximum = 5°); b) Inverse pole figure indicating micro-texture ($//X$).

This lack of banded microstructure may be the result of the post deposition heat treatment alleviating any subtle bimodal distribution, however, more work is required to investigate larger areas to compare directly to those previously published. An inhomogeneous microstructure was seen with discrete regions of smaller grains predominantly found in areas of smaller cross sectional area. This indicates the differing solidification rates between specimen thickness where areas of greater bulk act to retain thermal energy and increase the likelihood of grain nucleation mechanisms.

No distinct correlation could be determined between the deposition scan path and or layering effect with microstructure. Local misorientation maps which can give an indication of strain levels within the material, showed no abnormal major concentrations. Bands of higher misorientation were seen within grains and appeared to be in line with the lamellar structures which are more visible in the forward scatter images in Figure 10. It is unknown at this time whether the misorientation banding is affected by chosen deposition direction or strategy and is the focus of ongoing research.

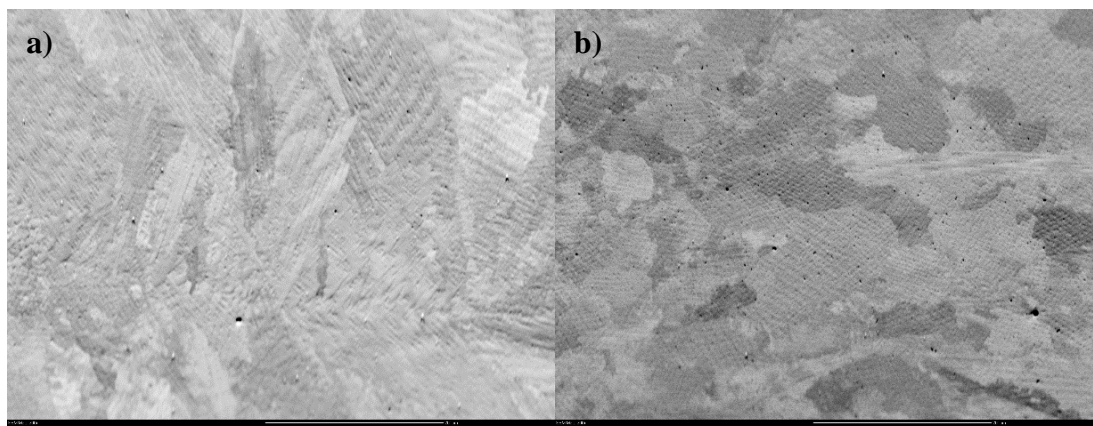


Figure 10: Forward scatter images of the microstructures of the two specimens, a) specimen #2 and b) specimen #6.

Heterogeneous microstructure, even on a fine length scale, can challenge mechanical performance predictions. Predicting bulk behaviour from samples of relatively small volume could lead to overly conservative estimates of statistical minimum values. Maps of property distribution could be considered as a means to account for statistical property minima, for example as a function of cooling rate.

Process maps based on solidification, repeat or dwell thermal exposure and cooling rate could be developed to control microstructural features via toolpaths and with consistent processing reduce the scatter in properties.

Conclusions

- The blown powder DLD component showed a low level of porosity, although isolated spherical micro-pores were found widely distributed with a maximum diameter of approximately 0.12mm.
- The microstructure as observed optically was consistent throughout the component and notably insensitive to wall thickness or orientation. Generally, a continuous, three dimensional cored γ " precipitation structure was evident. Some evidence of two dimensional arrays was noted.

- EDX measurements have confirmed a relatively high niobium content within the γ'' phase compared to the γ matrix. The EDX analysis of the present γ'' is consistent with data from a previous study on IN718 SMD materials containing δ - γ'' phases.
- Both primary and secondary dendrite arm spacing's were consistent with values found in the literature. Similar measurements were obtained when employing the conventional and novel triangular based techniques.
- The consistency of microstructure, coupled with a lack of detrimental phases and porosity, indicates that blown powder DLD is a tool that should be considered for selective applications. Whilst the process may come with a high capital cost, a high level of flexibility is ensured favouring high performance additive manufacturing applications

Acknowledgements

The authors would like to thank Rolls-Royce plc and for their technical support and guidance throughout this research project and Optomec for supplying the material and providing permission to report it.

References

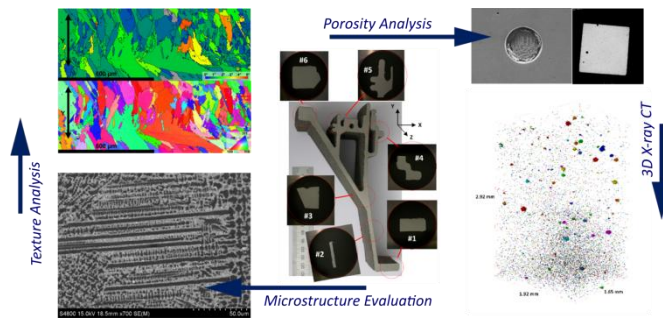
1. Durand-Charre, M., *The Microstructure of Superalloys*. 1998: Taylor & Francis.
2. Clark, D., M.R. Bache, and M.T. Whittaker, *Shaped metal deposition of a nickel alloy for aero engine applications*. *Journal of Materials Processing Technology*, 2008. **203**(1-3): p. 439-448.
3. Reed, R.C., *The Superalloys*. 2006: Cambridge University Press.
4. F. Brenne, T.N., H.J. Maier, *Additively manufactured cellular structures: Impact of microstructure and local strains on the monotonic and cyclic behavior under uniaxial and bending load*. *Journal of Materials Processing Tech*, 2013. **213**(9): p. 1558-1564.
5. Carroll, B.E., T.A. Palmer, and A.M. Beese, *Anisotropic tensile behavior of Ti-6Al-4V components fabricated with directed energy deposition additive manufacturing*. *Acta Materialia*, 2015. **87**: p. 309-320.

6. Lambarri, J., et al., *Microstructural and tensile characterization of Inconel 718 laser coatings for aeronautic components*. Optics and Lasers in Engineering, 2013. **51**(7): p. 813-821.
7. Zhang, D., et al., *Effect of standard heat treatment on the microstructure and mechanical properties of selective laser melting manufactured Inconel 718 superalloy*. Materials Science and Engineering: A, 2015. **644**: p. 32-40.
8. Wycisk, E., et al., *Effects of Defects in Laser Additive Manufactured Ti-6Al-4V on Fatigue Properties*. Physics Procedia, 2014. **56**: p. 371-378.
9. Bauereiß, A., T. Scharowsky, and C. Körner, *Defect generation and propagation mechanism during additive manufacturing by selective beam melting*. Journal of Materials Processing Technology, 2014. **214**(11): p. 2522-2528.
10. Gong, H., et al., *Analysis of defect generation in Ti-6Al-4V parts made using powder bed fusion additive manufacturing processes*. Additive Manufacturing, 2014. **1-4**: p. 87-98.
11. Cao, J., et al., *Effect of overlap rate on recrystallization behaviors of Laser Solid Formed Inconel 718 superalloy*. Optics & Laser Technology, 2013. **45**: p. 228-235.
12. Clark, D., M.R. Bache, and M.T. Whittaker, *Microstructural Characterization of a Polycrystalline Nickel-Based Superalloy Processed via Tungsten-Intert-Gas-Shaped Metal Deposition*. Metallurgical and Materials Transactions B, 2010. **41**(6): p. 1346-1353.
13. Fathi, A., et al., *Clad height control in laser solid freeform fabrication using a feedforward PID controller*. The International Journal of Advanced Manufacturing Technology, 2006. **35**(3): p. 280-292.
14. Zhu, G., et al., *The influence of laser and powder defocusing characteristics on the surface quality in laser direct metal deposition*. Optics & Laser Technology, 2012. **44**(2): p. 349-356.
15. Lin, J. and B.-C. Hwang, *Coaxial laser cladding on an inclined substrate*. Optics & Laser Technology, 1999. **31**(8): p. 571-578.
16. G. Bia, A.G., K. Wissenbach, A. Drenker, R. Poprawe, *Characterization of the process control for the direct laser metallic powder deposition*. Surface and Coatings Technology, 2006. **201**(6): p. 7.
17. Purtonen, T., A. Kalliosaari, and A. Salminen, *Monitoring and Adaptive Control of Laser Processes*. Physics Procedia, 2014. **56**: p. 1218-1231.
18. Reutzel, E.W. and A.R. Nassar, *A survey of sensing and control systems for machine and process monitoring of directed-energy, metal-based additive manufacturing*. Rapid Prototyping Journal, 2015. **21**(2): p. 159-167.
19. Tapia, G. and A. Elwany, *A Review on Process Monitoring and Control in Metal-Based Additive Manufacturing*. Journal of Manufacturing Science and Engineering 2014. **136**(6): p. 060801-060801.
20. Ahsan, M.N., R. Bradley, and A.J. Pinkerton, *Microcomputed tomography analysis of intralayer porosity generation in laser direct metal deposition and its causes*. Journal of Laser Applications, 2011. **23**(2): p. 022009.
21. Parimi, L.L., et al., *Microstructural and texture development in direct laser fabricated IN718*. Materials Characterization 2014. **89**: p. 102-111.
22. Paydas, H., et al., *Laser cladding as repair technology for Ti-6Al-4V alloy: Influence of building strategy on microstructure and hardness*. Materials & Design, 2015. **85**: p. 497-510.

23. Qiu, C., et al., *Fabrication of large Ti-6Al-4V structures by direct laser deposition*. Journal of Alloys and Compounds, 2015. **629**: p. 351-361.
24. Kong, C.Y., R.J. Scudamore, and J. Allen, *High-rate laser metal deposition of Inconel 718 component using low heat-input approach*. Physics Procedia, 2010. **5, Part A**: p. 379-386.
25. Liu, F., et al., *Microstructure and residual stress of laser rapid formed Inconel 718 nickel-base superalloy*. Optics & Laser Technology, 2011. **43**(1): p. 208-213.
26. Bache, M.R. and M.T. Whittaker, *Metallographic Characterisation of IN718 2003*, Rolls-Royce plc. Swansea, UTP.
27. DuPont, J.N., et al., *Solidification of Nb-bearing superalloys: Part II. Pseudoternary solidification surfaces*. Metallurgical and Materials Transactions A. **29**(11): p. 2797-2806.
28. Gäumann, M., et al., *Epitaxial laser metal forming: analysis of microstructure formation*. Materials Science and Engineering: A, 1999. **271**(1-2): p. 232-241.
29. Zonneveld, F.W. and W.N. Hanafee, *Computed Tomography of the Temporal Bone and Orbit*. Journal of Computer Assisted Tomography, 1988. **12**(3): p. 540.
30. Spoor, C.F., F.W. Zonneveld, and G.A. Macho, *Linear measurements of cortical bone and dental enamel by computed tomography: Applications and problems*. American Journal of Physical Anthropology, 1993. **91**(4): p. 469-484.
31. Bi, G., C.N. Sun, and A. Gasser, *Study on influential factors for process monitoring and control in laser aided additive manufacturing*. Journal of Materials Processing Technology 2013. **213**(3): p. 463-468.
32. Ma, M., Z. Wang, and X. Zeng, *Effect of energy input on microstructural evolution of direct laser fabricated IN718 alloy*. Materials Characterization 2015. **106**: p. 420-427.
33. Zhao, X., et al., *Study on microstructure and mechanical properties of laser rapid forming Inconel 718*. Materials Science and Engineering: A, 2008. **478**(1-2): p. 119-124.
34. Liu, F., et al., *Microstructural changes in a laser solid forming Inconel 718 superalloy thin wall in the deposition direction*. Optics & Laser Technology, 2013. **45**: p. 330-335.
35. Qian, L., *The influence of direct laser fabrication variables on microstructure of Ti6Al4V*. 2006, Birmingham.
36. S. Marimuthu, et al. *Finite Element Modelling of Substrate Thermal Distortion in Direct Laser Additive Manufacture of an Aero-Engine Component*. in *Institution of Mechanical Engineers, Part C: Journal of Mechanical Engineering Science*. 2012.
37. N.W. Klinbeil, C.J.B., S. Bontha, P.A. Kobryn, H.L.Fraser. *Prediction of Microstructure in Laser Deposition of Titanium Alloys*. in *Solid Freeform Fabrication Symposium*. 2002. University of Texas, Austin, USA.
38. Murty, A.D.P.a.Y.V. *Effect of Cooling Rate on Microstructural Development in Alloy 718 in Superalloys 718*. 2001.
39. Zhai, Y., D.A. Lados, and J.L. LaGoy, *Additive Manufacturing: Making Imagination the Major Limitation*. JOM, 2014. **66**(5): p. 808-816.
40. Kim, T.B., et al., *Additive manufactured porous titanium structures: Through-process quantification of pore and strut networks*. Journal of Materials Processing Technology, 2014. **214**(11): p. 2706-2715.

41. Zhou, X., et al., *3D-imaging of selective laser melting defects in a Co–Cr–Mo alloy by synchrotron radiation micro-CT*. *Acta Materialia*, 2015. **98**: p. 1-16.
42. Tamas-Williams, S., et al., *XCT analysis of the influence of melt strategies on defect population in Ti–6Al–4V components manufactured by Selective Electron Beam Melting*. *Materials Characterization*, 2015. **102**: p. 47-61.
43. Thijs, L., et al., *A study of the microstructural evolution during selective laser melting of Ti–6Al–4V*. *Acta Materialia*, 2010. **58**(9): p. 3303-3312.
44. Kobryn, P.A., E.H. Moore, and S.L. Semiatin, *The effect of laser power and traverse speed on microstructure, porosity, and build height in laser-deposited Ti6Al4V*. *Scripta Materialia*, 2000. **43**(4): p. 299-305.
45. Boisselier, D., S. Sankaré, and T. Engel, *Improvement of the Laser Direct Metal Deposition Process in 5-axis Configuration*. *Physics Procedia*, 2014. **56**: p. 239-249.
46. L. Renhof, C.K., E. Werner, M. Stockinger, *Analysis of microstructural properties of IN 718 after high speed forging*. TMS (The Minerals, Metals & Materials Society), 2005.
47. Amato, K.N., et al., *Microstructures and mechanical behavior of Inconel 718 fabricated by selective laser melting*. *Acta Materialia*, 2012. **60**(5): p. 2229-2239.
48. Ramirez, A.J., J.W. Sowards, and J.C. Lippold, *Improving the ductility-dip cracking resistance of Ni-base alloys*. *Journal of Materials Processing Technology*, 2006. **179**(1–3): p. 212-218.
49. Moat, R.J., et al., *Crystallographic texture and microstructure of pulsed diode laser-deposited Waspaloy*. *Acta Materialia*, 2009. **57**(4): p. 1220-1229.
50. Bland, S. and N.T. Aboulkhair, *Reducing porosity in additive manufacturing*. *Metal Powder Report*, 2015. **70**(2): p. 79-81.

Graphical abstract



ACCEPTED MANUSCRIPT

Highlights

- The novel manufacturing technique applied to an existing aerospace alloy has proved capable of providing a consistent microstructure in a complex geometry
- The blown powder DLD component showed a low level of porosity, although isolated spherical micro-pores were found widely distributed.
- The consistency of microstructure, coupled with a lack of detrimental phases and porosity, indicates that selected blown powder processes are tools that should be considered for appropriate structural geometries.
- Whilst the process may come with a high capital cost, a high level of flexibility is ensured favouring high performance additive manufacturing applications